Supporting Information for

Controlling Carrier Densities in Photochemically Reduced Colloidal ZnO Nanocrystals: Size Dependence and Role of the Hole Quencher

Alina M. Schimpf, Carolyn E. Gunthardt, Jeffrey D. Rinehart, James M. Mayer, and Daniel R. Gamelin*

Department of Chemistry, University of Washington, Seattle, WA 98195-1700, USA
**Electronic address: Gamelin@chem.washington.edu*

Electron counting

Electron counting was performed by titration against $[FeCp^*_2][BAr_F]$ ($[FeCp^*_2]^+$ = decamethylferrocenium, $[BAr_F]^-$ = tetrakis[3,5-bis(trifluoromethyl)phenyl]borate),[1,2] and analysis was conducted as described previously.[2] Addition of $[FeCp^*_2][BAr_F]$ removes electrons from the ZnO nanocrystals, as described by eq S1. Figure S1a plots NIR absorption spectra of photodoped r = 1.75 nm ZnO nanocrystals (TOPO-capped, 120 μM in 1:1 toluene/THF) at various stages of titration, using the NIR spectrum of the as-prepared nanocrystal solution as the baseline ($A_{difference} = A_{photodoped} - A_{as\text{-}prepared}$). With each addition of $[FeCp^*_2][BAr_F]$ to the photoreduced nanocrystals, the NIR absorption decreases due to nanocrystal oxidation. Once all of the ZnO electrons are removed, eq S1 can no longer proceed in the forward direction. Instead, further addition of $[FeCp^*_2][BAr_F]$ leads to growth of $[FeCp^*_2]^+$ absorption centered around ~700 nm (Figure S1b).

To determine $\langle n_{max} \rangle$, the decrease in NIR absorbance integrated from 800 to 1400 nm, and the subsequent increase in $[FeCp^*_2]^+$ absorption at 800 nm, are plotted versus equivalents of $[FeCp^*_2][BAr_F]$ added to the ZnO nanocrystals (Figure S1c). The x intercepts of these two lines indicate $\langle n_{max} \rangle$. The use of integrated absorption was found to be more reliable than the absorption at a single wavelength, but both yield similar results.[2] Often the number of electrons determined by the decrease in NIR absorption was slightly smaller than that determined by $[FeCp^*_2]^+$ absorption. The values reported here are averages of the two sides of the titration, and error bars encompass the upper and lower values. For r = 1.75 nm nanocrystals, $\langle n_{max} \rangle$ was determined to be 4.6 ± 0.6 e^-_{CB} per nanocrystal, which corresponds to an average maximum electron density of $\langle N_{max} \rangle = 1.9 \pm 0.3 \times 10^{20}$ cm^{-3}.

$$e^-_{CB}{:}ZnO + [FeCp^*_2]^+ \rightarrow ZnO + [FeCp^*_2] \qquad \text{(S1)}$$

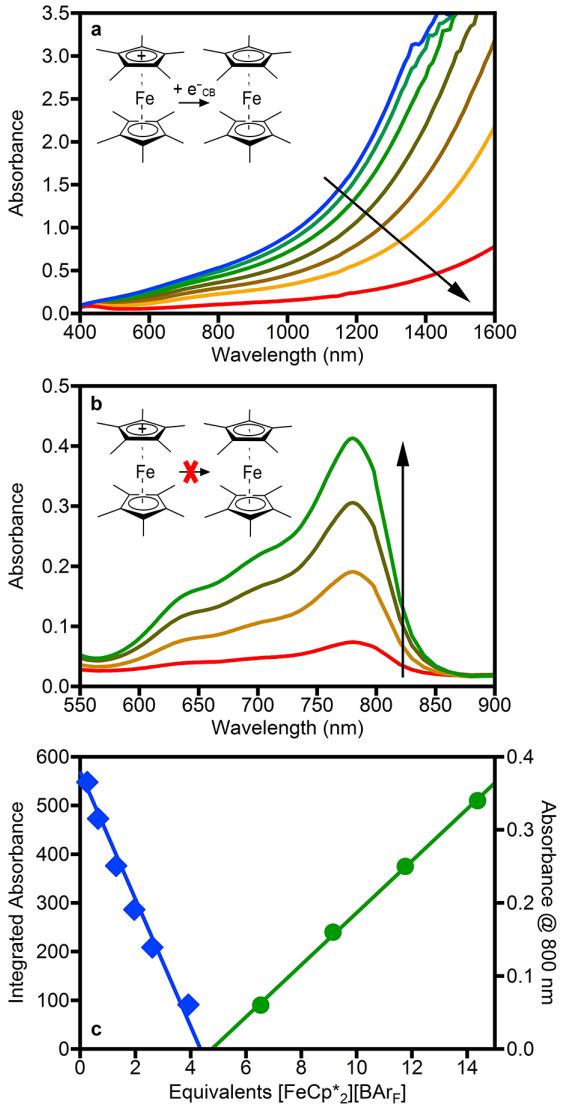

Figure S1. Absorption spectra of fully reduced r = 1.75 nm ZnO nanocrystals (top spectrum) with increasing amounts of $[FeCp^*_2][BAr_F]$ added, demonstrating (a) loss of the NIR absorption and (b) growth of $[FeCp^*_2]^+$ absorption. The arrows indicate increasing amounts of $[FeCp^*_2][BAr_F]$. (c) Integrated NIR absorption (800−1400 nm, blue diamonds) and $[FeCp^*_2]^+$ absorption at 800 nm (green circles) plotted as a function of $[FeCp^*_2][BAr_F]$ added to the NC solution. The solid lines are linear fits to the data. The equivalence point yields $\langle n_{max} \rangle$.

Table S1 summarizes the titration data for all of the nanocrystals described in Figure 2 of the main text, some of which are from previously published reports. The surface capping ligands and solvent are listed for each sample. All of these nanocrystals were reduced by photoexcitation in the presence of EtOH, but other experimental conditions were different. All of these samples follow the same trend in $\langle n_{max} \rangle$ versus r, as summarized in Figure 2 of the main text. Figure S2 replots the data in Figure 2 of the main text using symbols to represent the different surface ligands and solvents used in each experiment.

Table S1. Values for maximum number of electrons per nanocrystal and corresponding electron densities for the data presented in Figure 2 of the main text.

Radius	Ligand, Solvent	$\langle n_{max} \rangle$	$\langle N_{max} \rangle$ (10^{20} cm^{-3})	Ref.
1.75	TOPO, toluene/THF	4.6 ± 0.6	2.0 ± 0.3	this work
1.95	DDA, toluene/THF	4	1.3	1
2.15	TOPO, toluene/THF	5.0 ± 0.9	1.3 ± 0.3	this work
2.3	TOPO, toluene	5.7	1.1	3
2.5	Hydroxide, EtOH	10	1.5	4
2.8	TOPO, toluene/THF	16 ± 3	1.7 ± 0.4	this work
3.9	DDA, toluene/THF	42 ± 6	1.7 ± 0.3	this work
4.85	TOPO, toluene/THF	51 ± 7	1.0 ± 0.2	this work
5	DDA, toluene/THF	50	0.9	2
6.15	TOPO, toluene/THF	110 ± 20	1.4 ± 0.2	this work

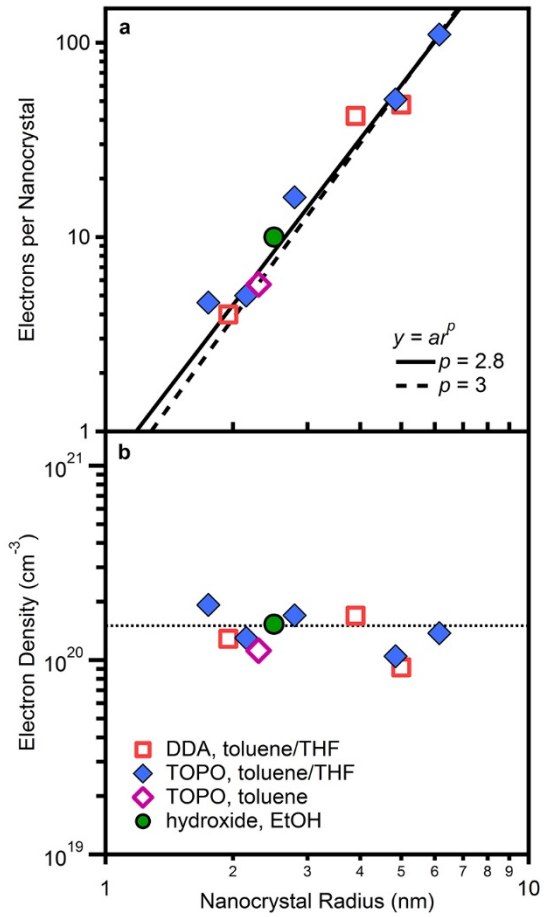

Figure S2. Size dependence of the maximum photodoping level in colloidal ZnO nanocrystals using EtOH as the hole quencher. **(a)** Maximum number of electrons per nanocrystal ($\langle n_{max} \rangle$) plotted versus nanocrystal radius on logarithmic scales. The red open squares are for DDA-capped nanocrystals suspended in 1:1 toluene THF. The solid blue diamonds are for TOPO-capped nanocrystals suspended in 1:1 toluene/THF. The open purple diamond is for TOPO-capped nanocrystals suspended in toluene. The filled green circle is for nanocrystals capped with hydroxides and suspended in EtOH. The solid line represents the best fit to eq 2 of the main text, which yields $p = 2.8$. The dashed line shows the best fit for $p = 3.0$. **(b)** The data from (a) re-plotted as the maximum electron density ($\langle N_{max} \rangle$) versus nanocrystal radius on logarithmic scales. The dotted line is the maximum carrier density averaged over all nanocrystal sizes ($\langle\langle N_{max} \rangle\rangle = 1.4 \pm 0.4 \times 10^{20}$ cm^{-3}).

Comparison between EtOH and hydride hole quenchers for photodoping of ZnO nanocrystals

Photodoping. A stock solution containing ~50 μM r = 2.15 nm ZnO nanocrystals (TOPO-capped in 1:1 toluene/THF) was prepared anaerobically. For photodoping with EtOH, 1 ml of the stock solution was combined with 1 ml THF. For photodoping with $LiEt_3BH$, 1 ml of the stock solution was combined with 1 ml of 10 mM $LiEt_3BH$ in THF. Both solutions were illuminated with UV light until the maximum photodoping level was reached.

Electron counting by titration with [FeCp*$_2$][BAr$_F$]. Both solutions were titrated as described above. The nanocrystals photodoped using EtOH were determined to have $\langle n_{max} \rangle$ = 5.4 e^-_{CB} per nanocrystal. Figure S2 shows the decrease in NIR absorption with added $[FeCp^*_2][BAr_F]$ for the ZnO nanocrystals irradiated in the presence of $Li[Et_3BH]$. The equivalence point of this titration yields $\langle n_{max} \rangle$ = 19 e^-_{CB} per nanocrystal, corresponding to 3.5 times more electrons than in the nanocrystals photodoped using EtOH. After complete loss of the NIR absorption, further addition of $[FeCp^*_2][BAr_F]$ did not lead to the expected linear increase in absorption of $[FeCp^*_2]^+$. We hypothesize that this result is due to direct reaction between $[FeCp^*_2][BAr_F]$ and the excess $Li[Et_3BH]$ when no more conduction band electrons are present in the nanocrystals.

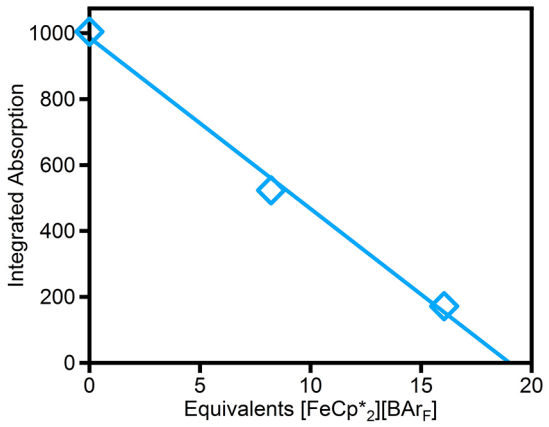

Figure S3. Integrated NIR absorption (800−1400 nm) plotted as a function of $[FeCp^*_2][BAr_F]$ added to the solution of ZnO nanocrystals photodoped using $Li[Et_3BH]$ as the hole quencher.

Electron counting by optical determination. To rule out the concern that reaction between $[FeCp^*_2][BAr_F]$ and excess $Li[Et_3BH]$ affects the decrease in NIR intensity, the number of

electrons in ZnO nanocrystals photodoped using $Li[Et_3BH]$ was also determined spectroscopically. Figure S3 shows absorption difference spectra ($A_{photodoped} - A_{as\text{-}prepared}$) for the fully photodoped nanocrystals prepared using EtOH (dotted blue line) and $Li[Et_3BH]$ (solid purple line). The ratio of integrated absorption between 800 and 1400 nm yields a ratio of 1:3.9 for the EtOH:$Li[Et_3BH]$ spectra, meaning that the nanocrystals reacted with $Li[Et_3BH]$ should contain ~22 e^-_{CB} per nanocrystal. These numbers agree well with those determined above by titration using $[FeCp^*_2][BAr_F]$ ($\langle n_{max} \rangle$ = 19 e^-_{CB} per nanocrystal, a ratio of 1:3.5 for the EtOH:$Li[Et_3BH]$ solutions), validating the use of such absorbance ratios for estimating the number of added electrons when photodoping with different hole quenchers.

The data in Figure 3 and Table 1 of the main text were obtained by analyzing the absorbance of nanocrystals photodoped using hydride hole quenchers relative to the same nanocrystals photodoped using EtOH. For the data presented in this figure and table, the nanocrystals photodoped using EtOH were assumed to have ($\langle N_{max} \rangle = 1.4 \pm 0.4 \times 10^{20}$ cm^{-3}, and the average carrier density of nanocrystals photodoped using a hydride was estimated by multiplying 1.4×10^{20} cm^{-3} by the ratio of integrated NIR absorption intensities. For example, if the integrated intensity between 800-1400 nm was three times more when photodoping was performed in the presence of $Li[Et_3BH]$ than in the presence of EtOH, the nanocrystals were estimated to have a maximum carrier density of $\langle N_{max} \rangle = 3 \times (1.4 \times 10^{20}$ $cm^{-3}) = 4.2 \times 10^{20}$ cm^{-3}. The estimated densities were then converted to numbers of electrons per nanocrystal.

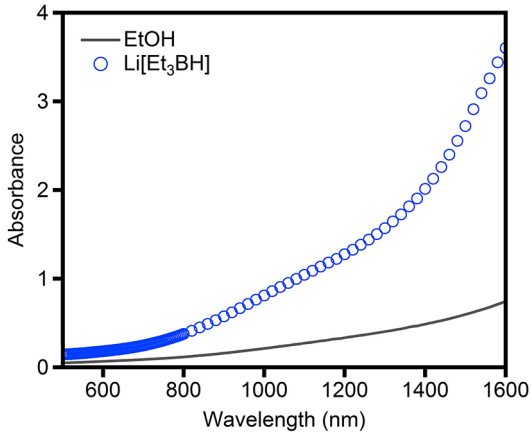

Figure S4. Absorption difference ($A_{photodoped}$ - $A_{as\text{-}prepared}$) of r = 2.15 nm ZnO nanocrystals photodoped to the maximum extent in the presence of EtOH (solid gray line) and $Li[Et_3BH]$ (blue circles).

Size dependence of the maximum photodoping level with various hole quenchers

The data in Fig. 3 of the main text, which describe the size dependence of the maximum photodoping using various hole quenchers, were fit to eq 2 of the main text. This was done both by holding $p = 3$, which facilitates interpretation of the fit paramater a in terms of the relative maximum electron density achieveble with each hole quencher. Fixing $p = 3$ biases the fitting slightly toward the larger nanocrystals, however, because in most cases these have slightly larger electron densities. Figure S5 shows fits of the same data, obtained when p is allowed to float. The values of p from these fits are summarized in Table S2, and in all cases are close to 3. This fitting was performed using a log-log representation of the data, but the data are presented on linear scales here for clarity.

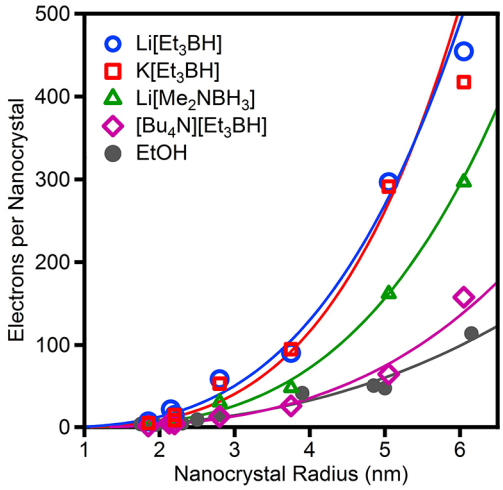

Figure S5. Size dependence of $\langle n_{max} \rangle$ of ZnO nanocrystals photodoped using various hole quenchers. The solid lines show fits to eq 2 of the main text in which p is allowed to float.

Table S2. Summary of the size dependence of ZnO nanocrystal photodoping using various hole quenchers. Parameters were obtained by fitting the data in Fig. 3b of the main text to eq 2 of the main text, allowing p to float.

ZQ	p
EtOH	2.7 ± 0.3
$[Bu_4N][Et_3BH]$	3.3 ± 0.3
$Li[Me_2NBH_3]$	3.5 ± 0.2
$K[Et_3BH]$	3.3 ± 0.4
$Li[Et_3BH]$	3.6 ± 0.4

Photodoping in the presence of acid

Figure S6 shows the NIR absorption spectra of TOPO-capped r = 2.8 nm ZnO nanocrystals photodoped using EtOH as the hole quencher, under different conditions. Sample **1** contains as prepared nanocrystals that were maximally photodoped (~3 h). To prepare sample **2,** the nanocrystals were fully photodoped, and to them added 10 equivalents of $[H(Et_2O)^+][BAr_F]$ (diethyl ether oxonium, $[BAr_F]^-$ = tetrakis[3,5-bis(trifluoromethyl)phenyl]borate).[5] This mixture was then photodoped for an additional 1 h. Sample **3** contains a mixture of as prepared nanocrystals and 10 equivalents of $[H(Et_2O)^+][BAr_F]$ that was maximally photodoped (~4 h). All samples contain the same concentration of nanocrystals in 1:1 toluene/THF. In contrast to chemically reduced nanocrystals,[5] added protons have no effect on the maximum number of electrons introduced photochemically by EtOH oxidation.

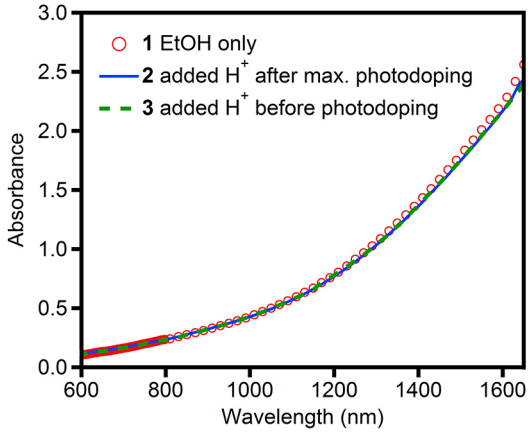

Figure S6. Comparison of NIR absorption spectra of TOPO-capped r = 2.8 nm ZnO nanocrystals photodoped using EtOH hole quencher, with and without additional acid, $[H(Et_2O)^+][BAr_F]$.

Analysis of photodoping kinetic data

Photodoping kinetic data (Fig. 5a of the main text) were fit to a double exponential (eq S2a) and initial rates determined by evaluating the initial slope (eq S2b). Tables S3a and S3b give a summary of the fitting parameters and analysis. The ratios $A_{max}^{ZQ}/A_{max}^{EtOH}$, which reflect $\langle N_{max}^{ZQ}\rangle/\langle N_{max}^{EtOH}\rangle$, are slightly smaller than the ratios $\langle\langle N_{max}^{ZQ}\rangle\rangle/\langle\langle N_{max}^{EtOH}\rangle\rangle$ obtained from analysis of the size dependence and reported in Table 1. This difference is likely due to two factors: (1) The absorbance values here are measured at a single wavelength, which may be

slightly different than the integrated intensities used in Table 1, and (2) these data represent only a single nanocrystal sample.

$$A = A_{\max} - A_1 e^{-k_1 t} - A_2 e^{-k_2 t} \tag{S2a}$$

$$R_0 = \left(\frac{dA}{dt} \right) \Bigg|_{t=0} = A_1 k_1 + A_2 k_2 \tag{S2b}$$

Table S3a. Summary of rate constants and weighting coefficients obtained from fitting kinetic data to eq S2a.

ZQ	A_1	k_1	A_2	k_2
EtOH	0.138 ± 0.007	0.037 ± 0.005	0.044 ± 0.007	0.9 ± 0.4
EtOH + $Li[PF_6]$	0.186 ± 0.004	0.078 ± 0.004	0.037 ± 0.004	4 ± 1
$[Bu_4N][Et_3BH]$	0.11 ± 0.02	8 ± 1	0.05 ± 0.02	30 ± 10
$Li[Me_2NBH_3]$	0.10 ± 0.01	4.6 ± 0.5	0.21 ± 0.01	25 ± 2
$Li[Et_3BH]$	0.29 ± 0.01	3.2 ± 0.5	0.30 ± 0.02	35 ± 3
$K[Et_3BH]$	0.26 ± 0.03	1.9 ± 0.4	0.32 ± 0.03	29 ± 5

Table S3b. Summary of initial rates and photodoping levels. Maximum photodoping levels were obtained from fitting kinetic data to eq S2a. Initial rates were obtained by evaluating eq S2b.

ZQ	R_0^{ZQ}	R_0^{ZQ} / R_0^{EtOH}	A_{max}^{ZQ}	$A_{max}^{ZQ} / A_{max}^{EtOH}$
EtOH	0.04 ± 0.02	1	0.21 ± 0.02	1
EtOH + $Li[PF_6]$	0.18 ± 0.05	4 ± 1	0.23 ± 0.02	1.1 ± 0.1
$[Bu_4N][Et_3BH]$	2 ± 1	50 ± 20	0.16 ± 0.01	0.8 ± 0.1
$Li[Me_2NBH_3]$	5.6 ± 5	130 ± 10	0.31 ± 0.2	1.5 ± 0.2
$Li[Et_3BH]$	11 ± 1	250 ± 30	0.59 ± 0.05	2.8 ± 0.3
$K[Et_3BH]$	10 ± 2	220 ± 40	0.59 ± 0.05	2.8 ± 0.3

Formation of Zn^0 metal

Figure S7 shows typical examples of the black/brown coloration observed in ZnO nanocrystal suspensions following exposure to UV illumination (~15 min) in the presence of excess (~500 equivalents) $Li[Et_3BH]$ or $Li[Me_2NBH_3]$. Experimental conditions were the same as described in the main text. When these samples were precipitated in air, X-ray diffraction (XRD) showed only ZnO, and Zn^0 was not detectable.

Figure S7. Coloration of ZnO nanocrystal suspensions when exposed to UV illumination in the presence of $Li[Et_3BH]$ or $Li[Me_2NBH_3]$.

Figure S8 shows the XRD pattern obtained for a drop-coated film of r = 3.75 nm ZnO nanocrystals before photodoping (top spectrum, dotted black line). Following extensive UV irradiation (24 h) of the colloids in the presence of excess $Li[Et_3BH]$ ($>10^4$ equivalents), coloration was observed, and a brown/black byproduct could be separated from the nanocrystals by centrifugation and washing with hexanes. The resultant pellet was placed between two pieces of Kapton tape and the XRD spectrum measured (bottom spectrum, solid black line). The patterns for ZnO and Zn^0 are shown at the bottom (blue and red, respectively). Before photodoping, the sample shows only ZnO peaks. The byproduct of photodoping shows both ZnO and Zn^0 metal peaks, plus some additional peaks that could be due to a Li_xZn intermetallic.[6] The large amorphous peak below 30 degrees is due to Kapton tape.

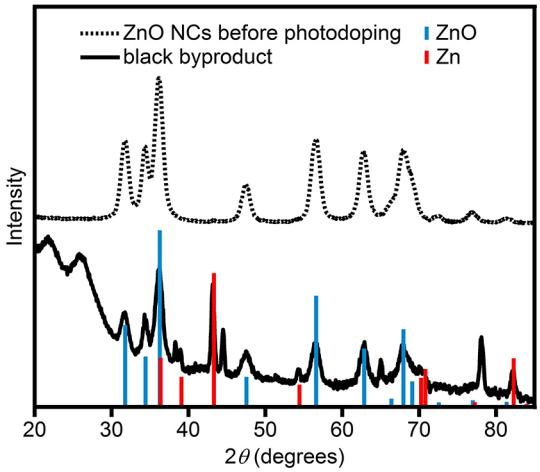

Figure S8. XRD spectra of r = 3.75 ZnO nanocrystals before photodoping (top spectrum, dotted black line) and of the black byproduct generated during photochemical doping with Li[Et_3BH]. The ZnO (blue) and Zn^0 (red) patterns are given for reference.

Stability of the photolysis lamp

The stability of the lamp used during the kinetics experiments was examined by monitoring the lamp output over time (data point taken every 10 s, averaged for 10 ms) using an Ocean Optics 2000+ fiber-coupled spectrometer. Figure S9a shows the lamp intensity (integrated from 340-380 nm) as a function of time. Figure S9b plots a histogram of the data in Figure S9a. The black curve shows a Gaussian fit to the data (eq S3), yielding a standard deviation that is ~8% of the mean. This difference is small compared to the differences in initial photodoping rates using EtOH and the hydride hole quenchers shown in Fig. 5 of the main text. Lamp intensity variations could possibly contribute to differences between initial photodoping rates among the different hydride hole quenchers or between those observed using EtOH with and without added Li[PF_6].

$$y = y_0 + A\exp\left(-\frac{(x-x_0)^2}{2\sigma^2}\right) \qquad \text{(S3)}$$

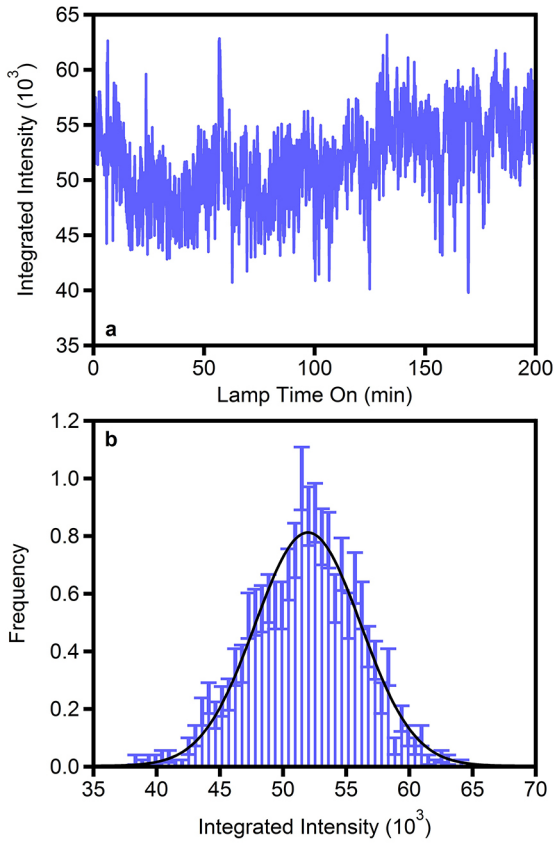

Figure S9. (a) Output of the UV photolysis lamp over time. Each data point represents the integrated intensity between 340−380 nm, averaged for 10 ms. A data point was collected every 10 s. **(b)** Histogram of data from (a). The solid black curve shows a Gaussian fit to the data, yielding a standard deviation that is ~8% of the mean.

References

(1) Schrauben, J.; Hayoun, R.; Valdez, C.; Braten, M.; Fridley, L.; Mayer, J. Titanium and zinc oxide nanoparticles are proton-coupled electron transfer agents. *Science* **2012**, *336*, 1298.

(2) Schimpf, A. M.; Ochsenbein, S. T.; Buonsanti, R.; Milliron, D. J.; Gamelin, D. R. Comparison of extra electrons in colloidal n-type Al^{3+}-doped and photochemically reduced ZnO nanocrystals. *Chem. Commun.* **2012**, *48*, 9352.

(3) Liu, W. K.; Whitaker, K. M.; Smith, A. L.; Kittilstved, K. R.; Robinson, B. H.; Gamelin, D. R. Room-temperature electron spin dynamics in free-standing ZnO quantum dots. *Phys. Rev. Lett.* **2007**, *98*, 186804.

(4) Wood, A.; Giersig, M.; Mulvaney, P. Fermi level equilibration in quantum dot-metal nanojunctions. *J. Phys. Chem. B* **2001**, *105*, 8810.

(5) Valdez, C. N.; Braten, M.; Soria, A.; Gamelin, D. R.; Mayer, J. M. Effect of protons on the redox chemistry of colloidal zinc oxide nanocrystals. *J. Am. Chem. Soc.* **2013**, *135*, 8492.

(6) Kushima, A.; Liu, X. H.; Zhu, G.; Wang, Z. L.; Huang, J. Y.; Li, J. Leapfrog cracking and nanoamorphization of ZnO nanowires during in situ electrochemical lithiation. *Nano Lett.* **2011**, *11*, 4535.